Monthly Notices of the ROYAL ASTRONOMICAL SOCIETY

MNRAS **525,** 3061–3074 (2023) https://doi.org/10.1093/mnras/stad2335
Advance Access publication 2023 August 4

Towards a reliable prediction of the infrared spectra of cosmic fullerenes and their derivatives in the *JWST* era

Jianzhi Xu,[1] Aigen Li,[2] Xiaohu Li[3] and Gao-Lei Hou [1]★

[1]*MOE Key Laboratory for Non-Equilibrium Synthesis and Modulation of Condensed Matter, School of Physics, Xi´an Jiaotong University, Shaanxi, Xi´an 710049, China*
[2]*Department of Physics and Astronomy, University of Missouri, Columbia, MO 65211, USA*
[3]*Xinjiang Astronomical Observatory, Chinese Academy of Sciences, Xinjiang, Urumqi 830011, China*

Accepted 2023 July 28. Received 2023 July 24; in original form 2023 June 29

ABSTRACT

Fullerenes, including C_{60}, C_{70}, and C_{60}^+, are widespread in space through their characteristic infrared vibrational features (C_{60}^+ also reveals its presence in the interstellar medium through its electronic transitions) and offer great insights into carbon chemistry and stellar evolution. The potential existence of fullerene-related species in space has long been speculated and recently put forward by a set of laboratory experiments of C_{60}^+, $C_{60}H^+$, $C_{60}O^+$, $C_{60}OH^+$, $C_{70}H^+$, and [C_{60}-Metal]$^+$ complexes. The advent of the *JWST* provides a unique opportunity to search for these fullerene-related species in space. To facilitate *JWST* search, analysis, and interpretation, accurate knowledge of their vibrational properties is essential. Here, we compile a VibFullerene database and conduct a systematic theoretical study on those species. We derive a set of range-specific scaling factors for vibrational frequencies to account for the deficiency of density functional theory calculations in predicting accurate frequencies. Scaling factors with low root-mean-square and median errors for the frequencies are obtained, and their performance is evaluated, from which the best-performing methods are recommended for calculating the infrared spectra of fullerene derivatives that balance the accuracy and the computational cost. Finally, the recommended vibrational frequencies and intensities of fullerene derivatives are presented for future *JWST* detection.

Key words: astrochemistry – molecular data – ISM: molecules – infrared: ISM.

1 INTRODUCTION

The discovery of fullerene in 1985, motivated by Sir Harold Kroto's curiosity about the formation mechanism of carbon-chain molecules in circumstellar envelopes, was a serendipitous event (Avery et al. 1976; Broten et al. 1978; Kroto et al. 1978, 1985). Later macroscopic synthesis of C_{60} enabled its spectroscopic characterization in both solid and vapour phases, providing laboratory reference to search for C_{60} potentially in space, as speculated by Kroto based on the high stability of C_{60} in harsh radiation conditions (Kroto et al. 1985; Kroto 1988). In 2010, Cami et al. made the first identification of circumstellar C_{60} through its infrared-active features at 7.0, 8.5, 17.4, and 18.9 μm in a young planetary nebula Tc 1 (Cami et al. 2010). Over the past decade, C_{60} has been detected in various astrophysical environments, including evolved stars, reflection nebulae, photodissociation regions, and the diffuse interstellar medium (ISM; García-Hernández et al. 2010, 2011a,b, 2012; ; Sellgren et al. 2010; Gielen et al. 2011; Zhang & Kwok 2011; Bernard-Salas et al. 2012; Peeters et al. 2012; Castellanos et al. 2014; Berné et al. 2017), suggesting that it is widely and abundantly spread in space (Woods 2020).

Fullerenes may also reveal their presence in space through their characteristic electronic transitions. Indeed, in 2015, Maier and co-workers measured the first high-resolution, gas-phase absorption spectrum of C_{60}^+ utilizing their newly developed cryogenic ion trap via helium-tagging technique (Campbell et al. 2015), and identified two strong features at 9577 and 9632 Å and three weak features at 9348, 9365, and 9428 Å (Campbell et al. 2015, 2016a,b; Campbell & Maier 2018), coincident with the mysterious diffuse interstellar bands at 9365, 9428, 9577, and 9632 DIBs as confirmed in 2019 by *Hubble Space Telescope* (Walker et al. 2016; Cordiner et al. 2019).

To date, C_{60}, C_{60}^+, and C_{70} are the largest molecules identified in space. C_{60} only has four active infrared features due to its I_h symmetry. Distorting the carbon cage by ionization or adsorption of foreign atoms or groups could reduce the symmetry and introduce more active infrared features. In fact, fullerenes undergo complicated chemical processing during stellar evolution, making the formation of hydrogenated fullerenes, fullerene-metal, and fullerene-hydrocarbon complexes possible (Kroto & Jura 1992; Cami 2014; Omont 2016; Zhang et al. 2020, 2022; Barzaga et al. 2022; Hou et al. 2023). Due to its high-spectral resolution and unprecedented sensitivity, the advent of the *JWST* offers a valuable opportunity to detect fullerene derivatives through their vibrational bands. This will allow us to quantitatively determine (or place an upper limit on) the presence and abundances of specific derivatives of fullerene in space. To this end, an accurate knowledge of the frequencies and intensities of the vibrational bands of fullerene derivatives is required.

Also, Gerlich et al. (2018) recently reported the gas-phase infrared spectrum of C_{60}^+ using He-tagging technique in the spectral range of 1100–1600 cm^{-1}, but without detailed explanation on the origin of the measured features. Oomens and co-workers measured the infrared spectra of gas-phase $C_{60}H^+$, $C_{60}O^+$, $C_{60}OH^+$, and

★ E-mail: lia@missouri.edu, gaolei.hou@xjtu.edu.cn

Table 1. Summary of fullerene-related species considered in VibFullerene (92*f*/7 mol) with chemical formulas, experimental methods, vibrational frequencies, number of frequencies, and references.

Formula	Method	Frequencies	Number	Ref.
C_{60}	FTIR	527, 577, 1183, 1429	4	Hare et al. (1991)
C_{70}	FTIR	533, 565, 575, 642, 669, 795, 1087, 1134, 1163, 1205, 1241, 1295, 1325, 1416, 1428, 1462, 1490, 1563	18	Schettino et al. (2002)
C_{60}^+	IR(M)PD	1173, 1178, 1191, 1216, 1222, 1307, 1327, 1402, 1544, 1560	10	Gerlich et al. (2018)
$C_{60}H^+$	IRMPD	524, 566, 756, 953, 1037, 1094, 1167, 1199, 1229, 1301, 1370, 1415, 1467, 1523, 1545	15	Palotás et al. (2019)
$C_{60}O^+$	IRMPD	519, 952, 1067, 1088, 1181, 1240, 1285, 1333, 1390, 1516	10	Palotás et al. (2022)
$C_{60}OH^+$	IRMPD	526, 573, 705, 760, 786, 958, 1029, 1088, 1173, 1195, 1232, 1296, 1328, 1411, 1468, 1526, 1540	17	Palotás et al. (2022)
$C_{70}H^+$	IRMPD	528, 570, 636, 665, 685, 723, 795, 821, 893, 933, 1065, 1160, 1208, 1304, 1368, 1434, 1498, 1543	18	Palotás et al. (2021)

$C_{70}H^+$, using the infrared multiple photon dissociation (IRMPD) spectroscopy (Palotás et al. 2019, 2021, 2022) and explored their possible relevance to the so-called 'unidentified infrared emission' (UIE) bands which are ubiquitously seen at 3.3, 6.2, 7.7, 8.6, and 11.3 μm in a wide range of astrophysical regions. These elegant but challenging laboratory experiments are essential to fully understand the astronomical observations. Theoretical simulations, in particular those based on density functional theory (DFT), have proved to be a superior complementary approach, on one hand to reveal the feature origin by comparing with experiment, and on the other hand to predict the infrared spectra of experimentally unstudied species (Scott & Radom 1996; Neese 2009; Candian et al. 2019; Kerkeni et al. 2022; Sadjadi et al. 2022). The prediction can either base on harmonic approximation, or use the more accurate but also more expensive anharmonic method. To achieve a reliable prediction using the much cheaper harmonic calculations, scaling factors have been developed for correcting the computed frequencies (Pople et al. 1993; Scott & Radom 1996; Zapata Trujillo & McKemmish 2023).

In this work, we systematically investigate the infrared spectral properties of several experimentally measured fullerene-related species, including C_{60}, C_{70}, C_{60}^+, $C_{60}O^+$, $C_{60}OH^+$, $C_{60}H^+$, and $C_{70}H^+$ (hereafter we call them the VibFullerene database), and compare them with those computed using several popular DFT methods. We provide a set of scaling factors for a variety of DFT methods that lead theoretical calculations to better match the experiments, which might be employed in the *JWST* era to compare with observational data to explore their potential presence in space. By making use of appropriate scaling factors, we aim to simulate the infrared spectra of fullerene derivatives with high reliability and low cost. Readers who are interested only in the vibrational frequencies and intensities for future *JWST* detection may wish to proceed directly to Section 5.

2 DATABASE COMPILATION

A benchmark database containing gas-phase infrared spectra is essential for obtaining the scaling factors and thus the simulation of other related species. Pople et al. previously built a database of scaling factors for the calculations at HF, MP2, QCISD, and DFT levels (Pople et al. 1993), Truhlar et al. collected a database for scaling the calculated vibrational frequencies (Alecu et al. 2010), and recently McKemmish et al. compiled an updated database, VIBFREQ1295 for the scaling factors of vibrational frequency calculations (Zapata Trujillo & McKemmish 2022). Those databases mainly contain small molecules of fewer than 15 atoms. In this work, we compile in Table 1 a VibFullerene database consisting of 7 fullerene-related species, i.e. C_{60}, C_{70}, C_{60}^+, $C_{60}O^+$, $C_{60}OH^+$, $C_{60}H^+$, and $C_{70}H^+$, totally 92 vibrational frequencies. The database contains information on the chemical formula, experimental method, vibrational frequencies, and the number of frequencies considered. We use the notation 92 *f*/7 mol to describe the VibFullerene database, where *f* and mol represent the total number of frequencies and molecules considered. We note here that C_{60} and C_{70} are from vapour phase FTIR measurements (Hare et al. 1991; Schettino et al. 2002), while others are from gas-phase infrared dissociation experiments.

The VibFullerene database can be used to investigate the distortion effect on the vibrational frequencies of fullerenes, and to validate theoretical models for calculating vibrational frequencies. It should be pointed out that due to the experimental challenge in measuring the gas-phase infrared spectra of large molecules like fullerenes and their derivatives, VibFullerene database currently only contains 7 molecules. We expect to expand the database to include more species in the future (Hou et al. 2021, 2023; German et al. 2022; Li et al. 2022; Vanbuel et al. 2020).

3 METHODOLOGY

All geometries in the VibFullerene database are fully optimized without symmetry constriction, using eight different DFT functionals, including BP86 (Perdew 1986; Becke 1988), BPW91 (Becke 1988; Perdew & Wang 1992), TPSSh (Tao et al. 2003), PBE0 (Adamo & Barone 1999), B3LYP (Stephens et al. 1994), M06 (Zhao & Truhlar 2008), M06-2X (Zhao & Truhlar 2008), and ωB97XD (Chai & Head-Gordon 2008a,b). Since vibrational frequencies are less affected by basis sets than by the specific functional (Pagliai et al. 2014), the geometric parameters of the species in VibFullerene database were compared using B3LYP functional in combination with several different basis sets, including 3-21G (Binkley et al. 1980), 4-31G (Ditchfield et al. 1971), 6-31G** (Ditchfield et al. 1971; Hehre et al. 1972; Hariharan & Pople 1973), 6-311G** (Krishnan et al. 1980), def2-SVP (Weigend & Ahlrichs 2005), and N07D (Barone et al. 2008), to choose the best basis set in the following frequency calculations considering both accuracy and efficiency. Note that 4-31G and N07D have been widely employed to investigate the infrared features of cosmic polycyclic aromatic hydrocarbons (PAHs). Frequency analysis was carried out to assure the optimized geometries to be real minima and to simulate the theoretical infrared spectra. Anharmonic spectrum was computed by generalized second-order vibrational perturbation theory (GVPT2) method (Barone 2005; Barone et al. 2014). All calculations were conducted with Gaussian 09 program package (Frisch et al. 2013).

Table 2. Comparison of characteristic bond length (Å) and computation cost (in seconds, s) of vibrational analysis of fullerene-related species in VibFullerene database using B3LYP functional combined with different basis sets.

Species	Bond[a]	3-21G	4-31G	6-31G**	6-311G**	def2-SVP	N07D	Reference values
C_{60}	C–C	1.460	1.457	1.453	1.451	1.455	1.454	1.458(6)[b]
	C=C	1.390	1.393	1.396	1.392	1.398	1.397	1.401(10)[b]
C_{70}	1	1.459	1.455	1.452	1.450	1.453	1.453	1.461(8)[c]
	2	1.392	1.394	1.397	1.394	1.400	1.398	1.388(17)[c]
	3	1.455	1.451	1.448	1.446	1.450	1.449	1.453(11)[c]
	4	1.384	1.386	1.389	1.385	1.391	1.390	1.386(25)[c]
	5	1.456	1.452	1.450	1.447	1.451	1.450	1.468(11)[c]
	6	1.437	1.436	1.434	1.431	1.436	1.435	1.425(14)[c]
	7	1.419	1.420	1.421	1.418	1.423	1.422	1.405(13)[c]
	8	1.474	1.473	1.471	1.469	1.472	1.472	1.538(19)[c]
$C_{60}H^+$	C–H	1.106	1.105	1.105	1.103	1.112	1.106	1.103[d]
$C_{60}O^+$	C–O	1.401	1.400	1.374	1.372	1.366	1.372	1.37[e]
$C_{70}H^+$	C–H	1.106	1.105	1.105	1.104	1.112	1.107	1.104[f]
Time (s)[g]		740	915	3189	9427	6692	58999	

[a]Notation of bond parameters of C_{70} is provided in Fig. A1 of the Appendix. [b, c]Electron diffraction data from refs. Hedberg et al. (1991, 1997). [d, e, f]Computational results from refs. Palotás et al. (2019, 2021, 2022). [g]Time is evaluated by frequency analysis of C_{60} on a 52-core SE24HIJTP workstation.

Scaling factors (SF) were determined by a least-square fitting procedure via minimizing the root mean square error (RMSE; Pople et al. 1993, Scott & Radom 1996)

$$\mathrm{SF} = \sum_i^N \omega_{i,\mathrm{theo}} \tilde{\nu}_{i,\mathrm{exp}} / \sum_i^N (\omega_{i,\mathrm{theo}})^2, \quad (1)$$

where $\omega_{i,\mathrm{theo}}$ and $\tilde{\nu}_{i,\mathrm{exp}}$ are ith theoretical and experimental frequencies, respectively, and N is the sum of all the considered vibrational modes in Table 1.

To evaluate the accuracy of the fitted scaling factors, we calculated the median errors as a more robust evaluation compared to RMSE, which can be significantly influenced by outliers (Zapata Trujillo & McKemmish 2022, 2023). Specifically, median errors refer to the median of the differences between the $\tilde{\nu}_{i,\mathrm{exp}}$ and $\lambda\omega_{i,theo}$.

It is found that theoretical frequencies are generally less overestimated in the low-frequency range than in the high-frequency region compared to the experimental fundamentals. Hence, a frequency-range-specific scaling approach (Zapata Trujillo & McKemmish 2023) is recommended to improve the accuracy of calculations. This method involves identifying an optimal segmentation point to separate the low-frequency and high-frequency ranges. The segmentation point with the least median error to separate the spectra into low- and high-frequency regions is searched for.

To quantitatively assess the agreement between the calculated and experimental infrared spectra, we employed the recently proposed cosine similarity score as an objective measure (Fu & Hopkins 2018; Kempkes et al. 2019; Müller et al. 2020). The cosine of the angle θ between two n-dimensional vectors is calculated using their normalized Euclidean dot product according to

$$\mathrm{Similarity} = \cos(\theta) = \frac{\mathbf{A}\cdot\mathbf{B}}{||\mathbf{A}||\,||\mathbf{B}||} = \frac{\sum_{i=1}^n A_i B_i}{\sqrt{\sum_{i=1}^n A_i^2}\cdot\sqrt{\sum_{i=1}^n B_i^2}}, \quad (2)$$

where $\mathbf{A}$ and $\mathbf{B}$ are two n-dimensional vectors with A_i and B_i as their i^{th} elements. This method assesses the degree to which the two vectors, representing the experimental and theoretical spectra in this case, are parallel. A cosine value closer to 1 indicates higher similarity. The intensity values in the computed spectrum are evaluated at the exact wavenumbers of the experimental spectrum, so that the two spectra have a common x-axis. To consider possible scaling for the calculated harmonic frequencies, the calculated spectra can be scaled first before calculating the cosine similarity scores.

Kempkes et al. proposed a slightly modified version of the above formula to make the cosine similarity scores more sensitive to the frequency overlap between bands in $\boldsymbol{A}$ and $\boldsymbol{B}$, and less to the deviations in their peak intensities (Kempkes et al. 2019). Both the experimental and calculated spectra are scaled to a maximum intensity of 1 and then the logarithm of these scaled values is taken as

$$\mathbf{A}_i^{rev} = \log\left(\frac{\mathbf{A}_i}{\mathbf{A}_{\max}} + c\right), \quad (3)$$

where c is a constant that is identical for vectors $\boldsymbol{A}$ and $\boldsymbol{B}$. The value of c is a compromise between being sensitive to low-intensity bands in the spectrum on the one hand and avoiding experimental noise affecting the similarity on the other hand. We followed this approach in the current work and used a c value of 0.71 by testing a small set of experimental and computational spectra to give the best results.

4 RESULTS

4.1 Geometric parameters

Table 2 compares the characteristic bond lengths of C_{60}, C_{70}, $C_{60}H^+$, $C_{60}O^+$, and $C_{70}H^+$ computed with different methods with those measured experimentally or computed theoretically (Hedberg et al. 1991, 1997; Palotás et al. 2019, 2021, 2022). It is shown that all the six basis sets are reasonable in reproducing the geometries of C_{60} and C_{70}, except that the experimental bond length of bond 8 of C_{70} is much longer (the notation of C_{70} bonds can be found in Fig. A1 of the Appendix). That is probably due to the elongation of equatorial bonds at high temperatures as employed in the experimental measurement.

It is noted that the polarization function is crucial for obtaining reliable structural results (Xu & Hou 2022), and 3-21G and 4-31G basis sets can lead to errors up to 0.03 Å, in particular for $C_{60}O^+$ in the calculations. Among the six basis sets, def2-SVP induces an error of approximately 1 percent when H atom is involved, as in the case of $C_{60}H^+$ and $C_{70}H^+$. The basis sets of 6-31G**, 6-311G**, and N07D, all yield satisfactory results. However, considering the computational cost of frequency analysis (Table 2), the 6-31G**

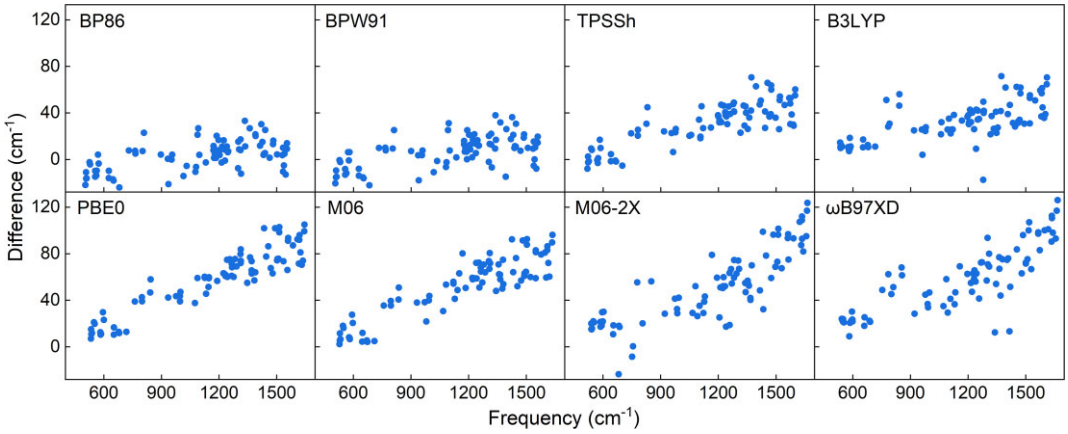

Figure 1. Distribution of the differences between the calculated harmonic and experimental frequencies in the full investigated spectral range. All calculations are performed with 6-31G** basis set.

basis set is recommended. This basis set was previously found to produce only minor errors in predicting the Raman and infrared modes of C_{60} (Pagliai et al. 2014).

4.2 Scaling factors

Theoretical infrared spectra based on harmonic approximation neglect anharmonic effects and often deviate from the experimental measurements for most hybrid functionals, and applying a uniform scaling factor in most cases could be able to correct the effect to a satisfactory extent (Pople et al. 1993). In Fig. 1, the distribution of differences between the calculated harmonic frequencies and experimental fundamentals are presented. For both BP86 and BPW91, the errors seem constant throughout the 400–1600 cm^{-1} spectral range, while for the other six hybrid functionals, the differences increase almost linearly with increasing wavenumber, calling for careful scaling of the calculated frequencies.

To obtain better agreement between the simulation and experiment, frequency-range-specific scaling factors would be desired as seen from the variations of the frequency differences in Fig. 1. We therefore fit sequentially in steps of 50 cm^{-1} over the entire spectral range to find the best segmentation point, and the results are summarized in Table A1 of the Appendix. It is shown that, compared with universal scaling factors, the median errors and RMSE are significantly reduced when the frequency-range-specific strategy is employed. We choose the segmentation point with the least median error to separate the spectra into low- and high-frequency regions. Note that some segmentation points with the least median error do not have the least RMSE values as RMSE is sensitive to outliers as explained in the Methodology section. The scaling factors are thus fitted separately for low- and high-frequency regions (Fig. 2), and the best-fitted scaling factors are summarized in Table 3. All R^2 values are larger than 0.997, suggesting satisfactory fittings. Note that some significant errors, such as that for the 795 cm^{-1} band of C_{70}, are not included and will be discussed in detail next. We note that the scaling factors obtained here for the high-frequency range are consistent with that previously obtained for small molecules (Scott & Radom 1996; Merrick et al. 2007; Alecu et al. 2010; Johnson 2022). It is also noted that the functionals with higher Hartree-Fock (HF) components tend to overestimate the calculated harmonic frequencies more, necessitating smaller scaling factors. For instance, the scaling factors for both BP86 and BPW91 in either low- or high-frequency range are close to unity, while for M06-2X with 54 percent HF component, scaling factors of 0.9631 and 0.9485 are required for the low- and high-frequency ranges, respectively.

Table 3 suggests that overall functionals with low-HF components exhibit smaller RMSE and median error values, and Fig. 3 presents the differences between the experimental fundamentals and the scaling-factor-corrected harmonic frequencies. It shows that either M06-2X or ωB97XD functionals may not be sufficiently robust, as a few frequencies exhibit deviations up to 40 cm^{-1}. A closer look at Fig. 3 finds some functional-dependent large absolute differences for certain vibrational modes, for which the vibrational vectors are provided in Fig. A2 of the Appendix. For example, BP86, BPW91, and M06 give the largest differences of 31, 26, and 25 cm^{-1}, respectively, for the coupling mode between tangential stretching of C_{60} and bending of C–O–H in $C_{60}OH^+$ with an experimental frequency of 958 cm^{-1}. For TPSSh, the significant difference is 30 cm^{-1} for the coupling mode between tangential stretching of C_{60} and C–C–H bending in $C_{60}H^+$ (exptl. 1301 cm^{-1}); for B3LYP, it is 31 cm^{-1} for the coupling mode between tangential stretching of C_{60} and C–O–H bending in $C_{60}OH^+$ (exptl. 786 cm^{-1}); and for PBE0, it is 26 cm^{-1} for the coupling mode between tangential stretching of C_{60} and C–O–C symmetrical stretching in $C_{60}O^+$ (exptl. 1333 cm^{-1}). These results highlight the origin of the large errors is due to the deficiency of harmonic calculations in predicting the vibrational coupling modes in the analysis. Decomposing these coupling modes to assess the influence of heteroatoms on the cage vibrational modes would be a valuable practice, as done previously (Hou et al. 2023), but is out of the scope of this work. Nonetheless, the errors due to the coupling modes generally fall in an acceptable range, emphasizing the potential of our approach to reliably predict the infrared spectra of fullerene-related species.

4.3 Verification of the performance of the fitted scaling factors

To test the performance of the fitted scaling factors, we generate a set of scaling-factor-corrected theoretical spectra and overlay them with the experimental spectra (Figs. 4 and A3 of the Appendix). An explicit comparison of the performance of different functionals using the cosine similarity score demonstrates the robustness of BP86 and BPW91 in predicting all fullerene-related species with high cosine similarity (Fu & Hopkins 2018; Kempkes et al. 2019; Müller et al. 2020). For sake of clarity, only spectra calculated with BP86/6-31G** are presented here, and others can be seen in Fig. A3 of the Appendix. Overall, good agreement is obtained between

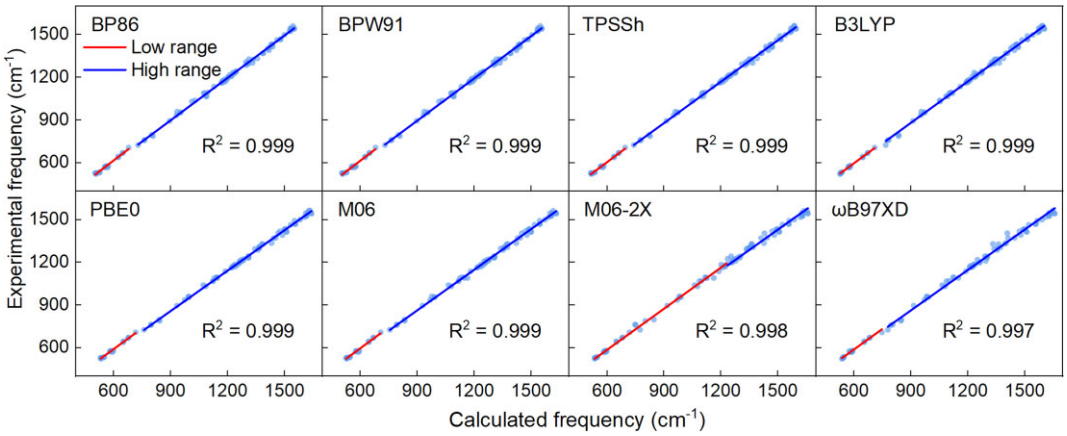

Figure 2. Scaling factors for the low- and high-frequency ranges of different functionals with 6-31G** basis set.

Table 3. Scaling factors obtained for different functionals with 6-31G** basis set.

Functionals (HF percent)	Scaling factors		RMSE	Med. error	Time (s)
BP86 (GGA)	1.0212 for <700 cm^{-1}	0.9941 for >700 cm^{-1}	10.2	5.3	1351
BPW91 (GGA)	1.0165 for <700 cm^{-1}	0.9905 for >700 cm^{-1}	10.7	5.5	1354
TPSSh (10 percent)	0.9972 for <700 cm^{-1}	0.9701 for >700 cm^{-1}	10.1	6.3	3321
B3LYP (20 percent)	0.9807 for <750 cm^{-1}	0.9697 for >750 cm^{-1}	11.0	5.2	3189
PBE0 (25 percent)	0.9755 for <750 cm^{-1}	0.9472 for >750 cm^{-1}	9.6	6.3	3390
M06 (27 percent)	0.9833 for <750 cm^{-1}	0.9519 for >750 cm^{-1}	10.6	7.0	4184
M06-2X (54 percent)	0.9631 for <1250 cm^{-1}	0.9485 for >1250 cm^{-1}	16.4	8.3	3702
ωB97XD	0.9635 for <750 cm^{-1}	0.9475 for >750 cm^{-1}	16.8	8.5	4407

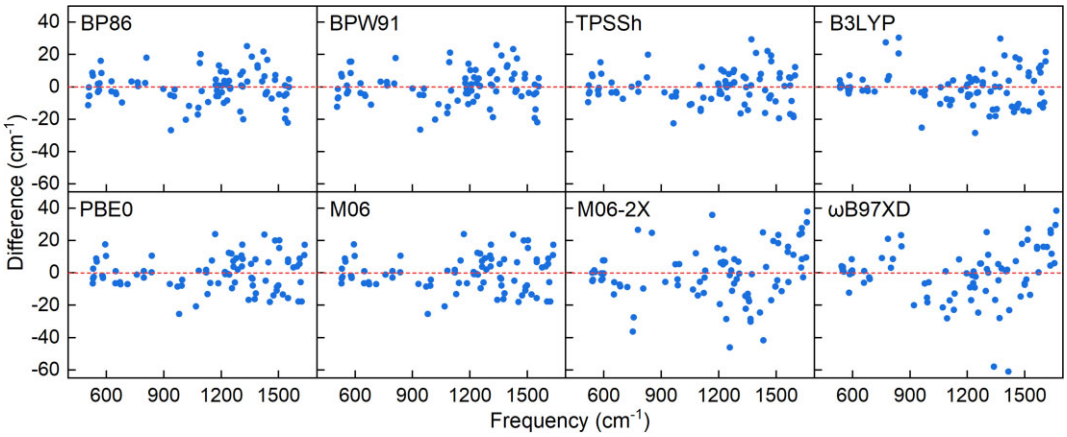

Figure 3. Distribution of frequency differences between the experimental fundamentals and the scaling-factor-corrected harmonic frequencies.

the corrected band frequencies and the experimental measurements except for several features of C_{60}^+ and C_{70}.

Fig. 4 shows that the scaled harmonic spectrum of C_{60} exhibits a good agreement with the FTIR measured spectrum regarding the vibrational frequencies, but the feature intensities exhibit some deviations. For $C_{60}H^+$ and $C_{60}O^+$, the theoretical spectra display stronger intensities around 520 cm^{-1}, which are identified as vibrational modes involving the radial breathing of the C_{60} cage (vibrational vectors can be seen in Fig. A2 of the Appendix). The theoretical spectrum of $C_{60}O^+$ also shows much stronger intensities than the IRMPD measurement in the spectral range of 1000–1500 cm^{-1}. The theoretical spectrum of $C_{60}OH^+$ shows large intensity deviations around 1400 cm^{-1} which involves tangential stretching and around 1000 cm^{-1} that mainly involves C–O stretching (Fig. A2 of the Appendix). The differences in intensities between calculations and experiments could be attributed to the non-linear effect due to multiple photon absorption, calling for more elegant infrared spectroscopy experiments in single-photon absorption scheme (Gerlich et al. 2018).

For C_{70}, a large discrepancy is found for the equatorial mode between the experimental frequency of 795 cm^{-1} and the theoretical value of 724 cm^{-1} (Fig. A2 of the Appendix), which has also been reported previously (Stratmann et al. 1998; Schettino et al. 2002; Pagliai et al. 2014; Palotás et al. 2021). Calculations including anharmonic effect fail to give a quantitative agreement on the frequency, presumably due to that the equatorial carbon atoms may be sensitive to temperature changes as higher temperatures during the experimental measurement may result in stronger vibrations of

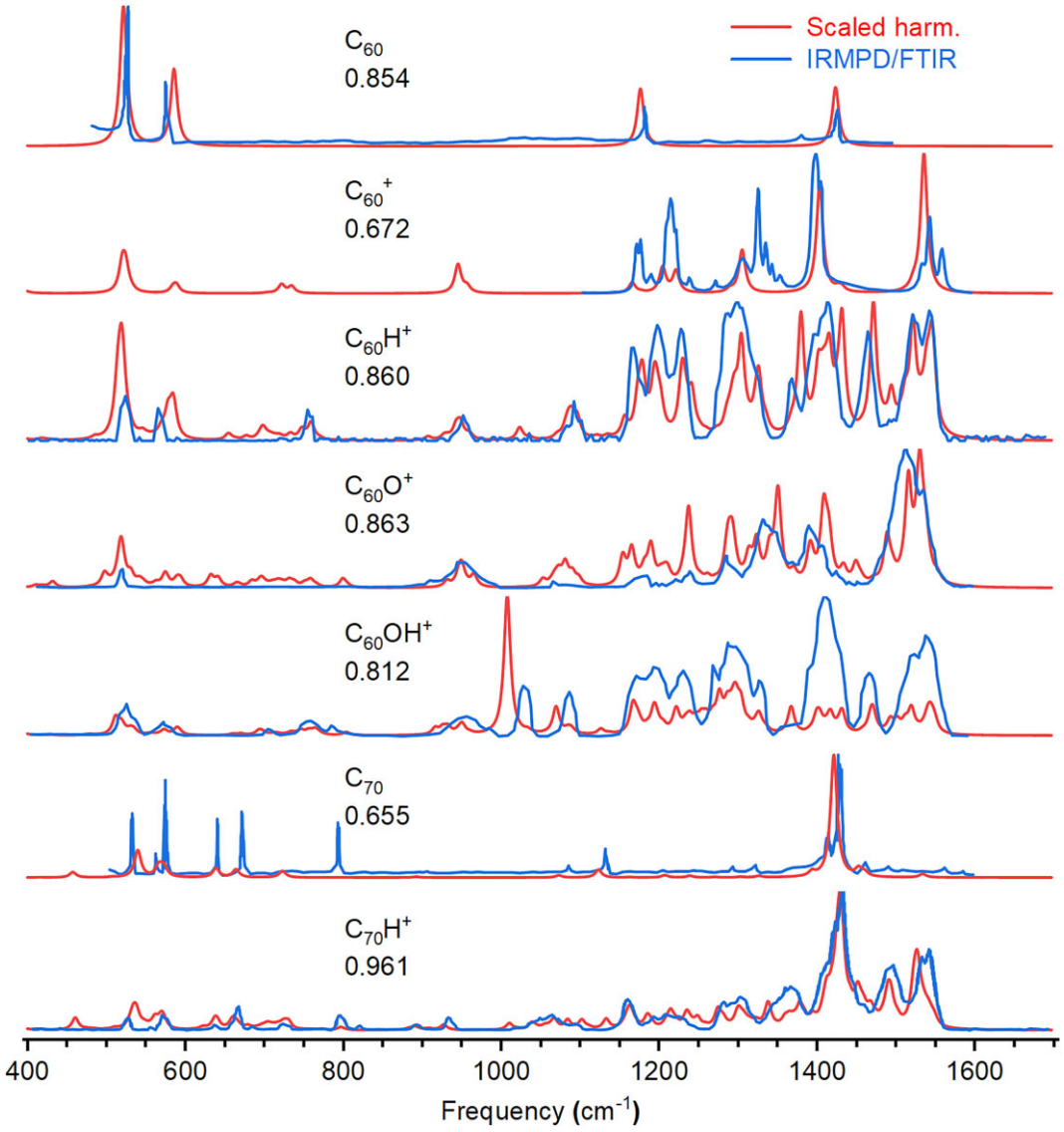

Figure 4. Scaled harmonic spectra at BP86/6-31G** and comparison with their experimental ones as digitized from refs. Hare et al. (1991), Schettino et al. (2002), Gerlich et al. (2018), and Palotás et al. (2019, 2021, 2022). The theoretical spectra are convolved using Lorentzian line shapes with full width at half maxima of 10 cm^{-1}. The cosine similarity score for each functional is indicated.

the equatorial belt compared to low temperatures (Hedberg et al. 1997).

The unsatisfactory comparison between the scaled harmonic spectrum of C_{60}^+ and experimental infrared photodissociation (IRPD) spectrum posts special attention as the experiment shows much richer features. Anharmonic effect could be one possible reason, and in Fig. 5, we present the calculated anharmonic and harmonic spectra of C_{60}^+, both at the BP86/6-31G** level, in addition to the experimental spectrum. The comparison shows that the fundamentals from anharmonic calculation exhibit a redshift compared to that from the harmonic calculation. Due to the lack of high-quality potential energy surface for C_{60}^+, the fundamental frequencies from anharmonic calculations may not be superior to the scaled harmonic calculations, as shown by large differences in some modes. The experimental features in the spectral range of 1200–1400 cm^{-1} may come from combination bands as suggested by the anharmonic calculations. However, the high cost of anharmonic calculation prohibits its application in general cases in predicting the infrared spectra of fullerene derivatives.

5 RECOMMENDATION FOR ASTROPHYSICAL APPLICATION

Table 2 demonstrates the suitability of 6-31G** basis set in predicting molecular geometries regarding both accuracy and computational cost, and detailed calculations with a range of DFT functionals suggest that functionals with low HF components, such as BP86, BPW91, TPSSh, B3LYP, PBE0, and M06, perform well in predicting the vibrational frequencies. In particular, the generalized gradient approximations (GGA), i.e. BP86 and BPW91, offer a good balance between the accuracy and computational efficiency, posting them interesting choices for simulating the infrared spectra of fullerene-related species. We note that the current work also validates the usefulness of the BPW91 functional in predicting the infrared spectra of $[C_{60}\text{-metal}]^+$ (metal = V and Fe) complexes (Hou et al. 2021, 2023). With the fitted scaling factors, excellent agreement is achieved between the simulated infrared spectra of $C_{60}V^+$ with laboratory measurements (Fig. A3 of the Appendix).

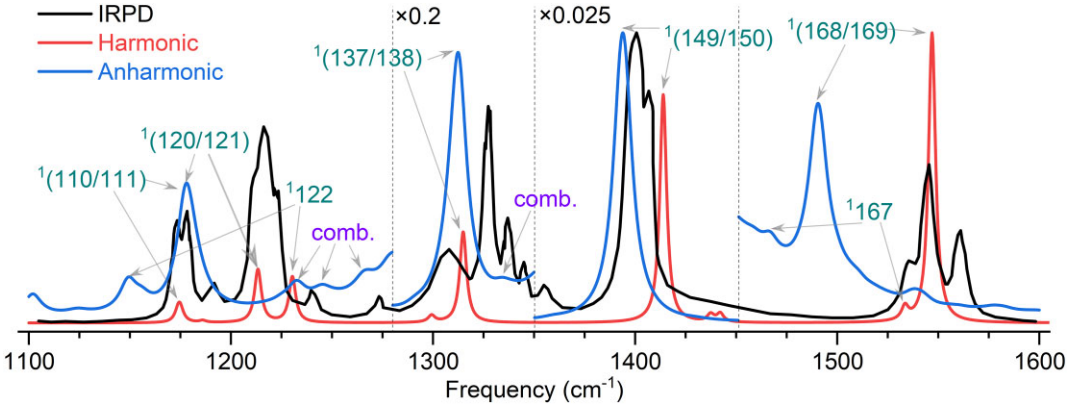

Figure 5. Simulated spectra of C_{60}^+ at BP86/6-31G** with harmonic approximation (red) and anharmonic effect (blue), convolved using Lorentzian line shapes of 10 cm^{-1} full width at half maximum. The experimental IRPD spectrum is digitized from Gerlich et al. (2018) and presented in black. The convolved anharmonic spectrum is scaled by a factor of 0.2 and 0.025 in the spectral range of 1280–1350 and 1350–1450 cm^{-1}, respectively. Tentative assignments of spectral features are provided with cyan and violet labels, corresponding to fundamental and combination bands, respectively.

In the *JWST* era, the high-sensitivity, high-resolution infrared spectral data would provide an unprecedented opportunity to identify specific species and to determine their abundances in space, or put upper limits on their abundances in case of non-detection. To this end, Table 4 summarizes the scaled harmonic frequencies and corresponding transition intensities of the fullerene derivatives. These data would be useful for exploring their cosmic relevance in comparison with astronomical data, in particular the upcoming higher quality *JWST* data. Nevertheless, it should be noted that conclusive identification of a specific species in space via those frequencies is still challenging, as pointed out previously (García-Hernández et al. 2010; Kwok, 2022; Hou, et al. 2023). For example, the features of fullerene derivatives at 7.7, 11.3, and 16.4 μm as shown in Table 4 could potentially coincide with the UIE bands often attributed to PAHs (Kwok 2022) by taking into account the frequency uncertainty. In addition, some features of the fullerene derivatives might even be hidden within the broad 6–9 and 11–13 μm emission plateaus (García-Hernández et al. 2010, 2011a; Kwok 2022; Hou et al. 2023). However, it might be advisible to realize that one should analyse the whole set of vibrational modes and their frequencies of a particular species to understand its cosmic relevance and importance, instead of relying on a specific band feature (Hou et al. 2023). With the unprecedented resolution and sensitivity of *JWST* in the 4.9–28.3 μm spectral range, distinguishing these species would become possible. It would be expected that such in-depth knowledge about the distinctive infrared signatures of these carbon species would undoubtedly contribute to our understanding of the organic inventory and carbon evolution in the universe.

6 CONCLUSIONS

We have conducted a systematic evaluation on the performance of common DFT functionals in predicting the infrared spectra of fullerenes and their derivatives. We have derived frequency-range-specific scaling factors for the functionals of BP86, BPW91, TPSSh, B3LYP, PBE0, M06, M06-2X, and ωB97XD, all with 6-31G** basis set. Overall, BP86 and BPW91 are recommended for simulating the infrared spectra of C_{60} and its derivatives regarding both their accuracy and computational efficiency. It is found that the coupling modes between the fullerene cage and the binding partner, in general are challenging to be accurately calculated. We also validated the reliability of the fitted factors by comparing the scaled theoretical and experimental infrared spectra of $[C_{60}$-Metal$]^+$ complexes, highlighting the usefulness of the current work and warranting the reliable prediction of potential fullerene-related species important in space. It is expected that the current result would greatly facilitate the analysis and interpretation of the upcoming *JWST* data particularly in the mid-infrared region covered by the mid-infrared instrument on board *JWST*.

ACKNOWLEDGEMENTS

This work was supported by National Natural Science Foundation of China (92261101) and the Innovation Capability Support Program of Shaanxi Province (2023-CX-TD-49). The authors acknowledge the support from the 'Young Talent Support Plan' of Xi'an Jiaotong University, the 'Excellent Overseas Young Scientist Program', 'Selective Funding Project for Overseas Student Scientific and Technological Activities' of Shaanxi province, China, as well as the Fundamental Research Funds for Central Universities, China. AL is supported in part by NASA grants (80NSSC19K0572 and 80NSSC19K0701). Part of the computational resources and services used in this work were provided by the VSC (Flemish Supercomputer Center), funded by the Research Foundation-Flanders (FWO) and the Flemish Government-department EWI. G-LH conceived and designed the work, JX conducted the work, JX, G-LH, and AL wrote the manuscript with comments from all authors, and G-LH obtained the funding for this research. All authors have given approval to the final version of the manuscript.

DATA AVAILABILITY

The data underlying this article is available in the article. Any inquiry about further details can be addressed to G.-L.H.

Table 4. Recommended frequencies and intensities of fullerene derivatives in the spectral range of 400–1600 cm^{-1} calculated at BP86/6-31G** level.

Species	ν/cm^{-1}	$\lambda/\mu m$	A/km mol^{-1}
C_{60}	522	19.2	22.1
	586	17.1	11.9
	1178	8.5	8.4
	1426	7.0	9.1
C_{70}	458	21.8	6.9
	540	18.5	7.0
	567	17.6	7.3
	573	17.5	12.9
	639	15.6	6.0
	665	15.0	5.4
	724	13.8	3.9
	1074	9.3	1.5
	1124	8.9	9.9
	1209	8.3	1.9
	1241	8.1	1.2
	1305	7.7	0.4
	1328	7.5	1.9
	1396	7.2	3.0
	1424	7.0	79.2
	1463	6.8	2.6
	1536	6.5	2.1
C_{60}^+	525	19.0	15.2
	589	17.0	5.3
	723	13.8	3.0
	736	13.6	2.4
	946	10.6	9.6
	1168	8.6	3.7
	1206	8.3	8.9
	1223	8.2	15.0
	1307	7.7	15.1
	1406	7.1	37.4
	1538	6.5	48.6
$C_{60}H^+$	520	19.2	16.1
	547	18.3	1.3
	569	17.6	1.2
	578	17.3	6.2
	656	15.2	1.5
	748	13.4	2.5
	760	13.2	2.6
	949	10.5	3.2
	1025	9.8	3.2
	1097	9.1	4.7
	1157	8.6	4.6
	1175	8.5	8.1
	1180	8.5	11.2
	1195	8.4	9.9
	1231	8.1	14.6
	1306	7.7	23.1
	1328	7.5	14.7
	1381	7.2	30.8
	1403	7.1	13.2
	1418	7.1	10.9
	1433	7.0	24.8
	1474	6.8	17.8
	1523	6.6	27.3
	1548	6.5	17.9
$C_{60}O^+$	432	23.1	2.3
	498	20.1	4.7
	518	19.3	8.6
	531	18.8	2.7
	575	17.4	3.9
	594	16.8	2.7
	633	15.8	4.1
	642	15.6	3.1
	684	14.6	2.1
	759	13.2	2.6
	800	12.5	3.2
	932	10.7	2.2
	951	10.5	7.3
	966	10.4	4.4
	1074	9.3	4.4
	1083	9.2	7.9
	1092	9.2	4.2
	1167	8.6	12.0
	1191	8.4	13.0
	1213	8.2	4.1
	1239	8.1	28.5
	1290	7.8	11.2
	1295	7.7	14.6
	1315	7.6	7.7
	1326	7.5	14.2
	1353	7.4	28.0
	1393	7.2	9.2
	1411	7.1	25.9
	1418	7.1	12.4
	1451	6.9	7.3
	1491	6.7	17.0
	1518	6.6	36.0
	1529	6.5	5.8
	1541	6.5	9.5
$C_{60}OH^+$	519	19.3	10.0
	535	18.7	3.5
	575	17.4	2.2
	589	17.0	5.0
	670	14.9	1.7
	694	14.4	3.7
	713	14.0	1.0
	734	13.6	1.7
	765	13.1	5.1
	805	12.4	2.9
	917	10.9	6.2
	927	10.8	6.1
	952	10.5	6.3
	1009	9.9	137.9
	1070	9.3	24.5
	1088	9.2	3.6
	1128	8.9	5.3
	1169	8.6	27.2
	1195	8.4	17.1
	1224	8.2	12.5
	1240	8.1	11.5
	1255	8.0	12.0
	1262	7.9	10.8
	1270	7.9	11.4
	1278	7.8	32.4
	1288	7.8	19.0
	1305	7.7	24.3
	1328	7.5	15.6
	1369	7.3	24.2
	1401	7.1	14.1
	1419	7.0	16.6
	1433	7.0	16.9
	1473	6.8	20.6
	1495	6.7	12.2
	1521	6.6	23.1
	1548	6.5	10.7
$C_{70}H^+$	461	21.7	6.7
	538	18.6	7.8
	572	17.5	5.1
	637	15.7	4.0
	660	15.2	4.5

Table 4 – *continued*

Species	ν/cm^{-1}	λ /μm	A/km mol^{-1}
	680	14.7	1.7
	697	14.3	1.0
	724	13.8	1.3
	731	13.7	1.3
	798	12.5	1.6
	891	11.2	1.2
	928	10.8	3.0
	1012	9.9	3.5
	1040	9.6	3.5
	1057	9.5	1.3
	1069	9.4	5.4
	1086	9.2	5.0
	1103	9.1	4.9
	1135	8.8	5.5
	1163	8.6	5.3
	1186	8.4	6.4
	1216	8.2	4.0
	1237	8.1	6.4
	1250	8.0	5.0
	1276	7.8	7.0
	1301	7.7	4.5
	1340	7.5	8.8
	1367	7.3	4.3
	1380	7.2	10.2
	1414	7.1	14.6
	1432	7.0	24.0
	1453	6.9	15.1
	1469	6.8	7.1
	1491	6.7	9.8
	1529	6.5	20.4
$C_{60}V^+$	417	24.0	1.8
	445	22.5	5.3
	511	19.6	5.2
	522	19.2	12.0
	582	17.2	11.3
	605	16.5	1.3
	697	14.3	1.1
	719	13.9	1.3
	952	10.5	1.1
	1081	9.3	2.1
	1168	8.6	4.7
	1177	8.5	7.8
	1190	8.4	4.5
	1235	8.1	1.7
	1283	7.8	2.3
	1305	7.7	1.0
	1323	7.6	1.4
	1378	7.3	6.3
	1406	7.1	7.1
	1411	7.1	7.4
	1426	7.0	16.7
	1469	6.8	6.7
	1500	6.7	6.3
	1517	6.6	17.2
	1529	6.5	7.6
	1548	6.5	1.5

REFERENCES

Adamo C., Barone V., 1999, J. Chem. Phys., 110, 6158
Alecu I., Zheng J., Zhao Y., Truhlar D. G., 2010, J. Chem. Theory Comput., 6, 2872
Avery L., Broten N., MacLeod J., Oka T., Kroto H., 1976, ApJ, 205, L173
Barone V., 2005, J. Chem. Phys., 122, 014108
Barone V., Biczysko M., Bloino J., 2014, Phys. Chem. Chem. Phys., 16, 1759
Barone V., Cimino P., Stendardo E., 2008, J. Chem. Theory Comput., 4, 751
Barzaga R., García-Hernández D., Díaz-Tendero S., Sadjadi S., Manchado A., Alcami M., 2022, ApJ, 942, 5
Becke A. D., 1988, Phys. Rev. A, 38, 3098
Bernard-Salas J., Cami J., Peeters E., Jones A., Micelotta E., Groenewegen M., 2012, ApJ, 757, 41
Berné O., Cox N., Mulas G., Joblin C., 2017, A&A, 605, L1
Binkley J. S., Pople J. A., Hehre W. J., 1980, J. Am. Chem. Soc., 102, 939
Broten N., Oka T., Avery L., MacLeod J., Kroto H., 1978, ApJ, 223, L105
Cami J., 2014, in Cami J., Cox N.L.J., eds., Proc. IAU Symp. 297, The Diffuse Interstellar Bands. Cambridge Univ. Press, Cambridge, p. 370
Cami J., Bernard-Salas J., Peeters E., Malek S. E., 2010, Science, 329, 1180
Campbell E. K., Holz M., Gerlich D., Maier J. P., 2015, Nature, 523, 322
Campbell E., Holz M., Maier J., 2016a, ApJ, 826, L4
Campbell E., Holz M., Maier J., Gerlich D., Walker G., Bohlender D., 2016b, ApJ, 822, 17
Campbell E. K., Maier J. P., 2018, ApJ, 858, 36
Candian A., Gomes Rachid M., MacIsaac H., Staroverov V. N., Peeters E., Cami J., 2019, MNRAS, 485, 1137
Castellanos P., Berné O., Sheffer Y., Wolfire M. G., Tielens A. G., 2014, ApJ, 794, 83
Chai J.-D., Head-Gordon M., 2008a, Phys. Chem. Chem. Phys., 10, 6615
Chai J.-D., Head-Gordon M., 2008b, J. Chem. Phys., 128, 084106
Cordiner M. et al., 2019, ApJ, 875, L28
Ditchfield R., Hehre W. J., Pople J. A., 1971, J. Chem. Phys., 54, 724
Frisch M. J. et al., 2013, Gaussian 09 Reversion E.01, Gaussian Inc., Wallingford CT
Fu W., Hopkins W. S., 2018, J. Phys. Chem. A, 122, 167
García-Hernández D. A., Manchado A., García-Lario P., Stanghellini L., Villaver E., Shaw R., Szczerba R., Perea-Calderón J., 2010, ApJ, 724, L39
García-Hernández D. A., et al., 2011a, ApJ, 737, L30
García-Hernández D. A., Rao N. K., Lambert D. L., 2011b, ApJ, 729, 126
García-Hernández D. A., Villaver E., García-Lario P., Acosta-Pulido J. A., Manchado A., Stanghellini L., Shaw R. A., Cataldo F., 2012, ApJ, 760, 107
Gerlich D., Jašík J., Strelnikov D. V., Roithová J., 2018, ApJ, 864, 62
German E., Hou G.-L., Vanbuel J., Bakker J. M., Alonso J. A., Janssens E., López M. J., 2022, Carbon, 197, 535
Gielen C., Cami J., Bouwman J., Peeters E., Min M., 2011, A&A, 536, A54
Hariharan P. C., Pople J. A., 1973, Theor. Chim. Acta, 28, 213
Hedberg K., Hedberg L., Bethune D. S., Brown C., Dorn H., Johnson R. D., De Vries M., 1991, Science, 254, 410
Hedberg K., Hedberg L., Bühl M., Bethune D. S., Brown C., Johnson R. D., 1997, J. Am. Chem. Soc., 119, 5314
Hehre W. J., Ditchfield R., Pople J. A., 1972, J. Chem. Phys., 56, 2257
Hou G.-L., Yang T., Li M., Vanbuel J., Lushchikova O. V., Ferrari P., Bakker J. M., Janssens E., 2021, Angew. Chem. Int. Ed., 60, 27095
Hou G.-L., Lushchikova O. V., Bakker J. M., Lievens P., Decin L., Janssens E., 2023, ApJ, 952, 13
Hare. J. P., Dennis T. J ., Kroto H. W., 1991, in Taylor R., Allaf A. W., Balm S., Walton D. R. M., eds, J. Chem. Soc., Chem. Commun., p. 412
Kempkes L. J., Martens J., Berden G., Houthuijs K. J., Oomens J., 2019, Faraday Discuss., 217, 434
Kerkeni B., García-Bernete I., Rigopoulou D., Tew D. P., Roche P. F., Clary D. C., 2022, MNRAS, 513, 3663
Krishnan R., Binkley J. S., Seeger R., Pople J. A., 1980, J. Chem. Phys., 72, 650
Kroto H. W., 1988, Science, 242, 1139
Kroto H. W., Jura M., 1992, A&A, 263, 275
Kroto H. W., Kirby C., Walton D., Avery L., Broten N., MacLeod J., Oka T., 1978, ApJ, 219, L133
Kroto H. W., Heath J. R., O'Brien S. C., Curl R. F., Smalley R. E., 1985, Nature, 318, 162
Kwok S., 2022, Astrophys. Space Sci., 367, 16
Li M., Yang T., Bakker J. M., Janssens E., Hou G.-L., 2022, Cell Rep. Phys. Sci., 3, 100910
Merrick J. P., Moran D., Radom L., 2007, J. Phys. Chem. A, 111, 11683

Müller F., Stückrath J. B., Bischoff F. A., Gagliardi L., Sauer J., Debnath S., Jorewitz M., Asmis K. R., 2020, J. Am. Chem. Soc., 142, 18050
Neese F., 2009, Coord. Chem. Rev., 253, 526
Omont A., 2016, A&A, 590, A52
Pagliai M., Cardini G., Cammi R., 2014, J. Phys. Chem. A, 118, 5098
Palotás J., Martens J., Berden G., Oomens J., 2019, Nat. Astron, 4, 240
Palotás J., Martens J., Berden G., Oomens J., 2021, ApJ, 909, L17
Palotás J., Martens J., Berden G., Oomens J., 2022, J. Phys. Chem. A, 126, 2928
Peeters E., Tielens A. G., Allamandola L. J., Wolfire M. G., 2012, ApJ, 747, 44
Perdew J. P., 1986, Phys. Rev. B, 33, 8822
Perdew J. P., Wang Y., 1992, Phys. Rev. B, 45, 13244
Pople J. A., Scott A. P., Wong M. W., Radom L., 1993, Isr. J. Chem., 33, 345
Johnson R. D.III, 2022, NIST Computational Chemistry Comparison and Benchmark Database. NIST Standard Reference Database Number 101. Release 22, May 2022, https://cccbdb.nist.gov/
Sadjadi S., Parker Q. A., Hsia C.-H., Zhang Y., 2022, ApJ, 934, 75
Schettino V., Pagliai M., Cardini G., 2002, J. Phys. Chem. A, 106, 1815
Scott A. P., Radom L., 1996, J. Phys. Chem., 100, 16502
Sellgren K., Werner M. W., Ingalls J. G., Smith J., Carleton T., Joblin C., 2010, ApJ, 722, L54
Stephens P. J., Devlin F. J., Chabalowski C. F., Frisch M. J., 1994, J. Phys. Chem., 98, 11623
Stratmann R. E., Scuseria G. E., Frisch M. J., 1998, J. Raman Spectrosc., 29, 483
Tao J., Perdew J. P., Staroverov V. N., Scuseria G. E., 2003, Phys. Rev. Lett., 91, 146401
Vanbuel J., Germán E., Libeert G., Veys K., Moens J., Alonso J. A., López M. J., Janssens E., 2020, ChemPhysChem, 21, 1012
Walker G., Campbell E., Maier J., Bohlender D., Malo L., 2016, ApJ, 831, 130
Weigend F., Ahlrichs R., 2005, Phys. Chem. Chem. Phys., 7, 3297
Woods P., 2020, Nat. Astron., 4, 299
Xu J., Hou G.-L., 2022, Phys. Rev. A, 106, 056801
Zapata Trujillo J. C., McKemmish L. K., 2022, J. Phys. Chem. A, 126, 4100
Zapata Trujillo J. C., McKemmish L. K., 2023, J. Phys. Chem. A, 127, 1715
Zhang C., Hu X., Yang Y., Chen Y., Zhen J., Qin L., 2022, A&A, 662, A21
Zhang Y., Kwok S., 2011, ApJ, 730, 126
Zhang Y., Sadjadi S., Hsia C.-H., 2020, Ap&SS, 365, 67
Zhao Y., Truhlar D. G., 2008, Theor. Chem. Acc., 120, 215

APPENDIX

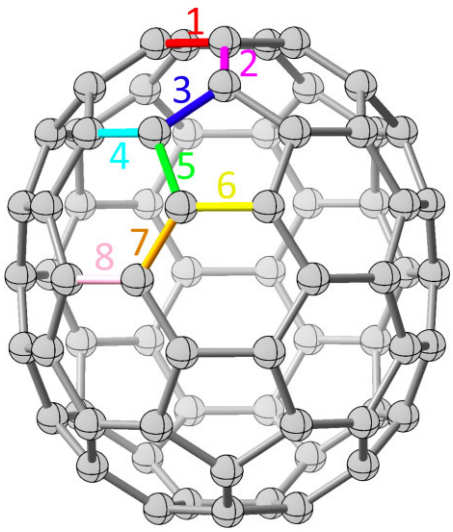

Figure A1. Notation of the C_{70} characteristic bonds in different colors.

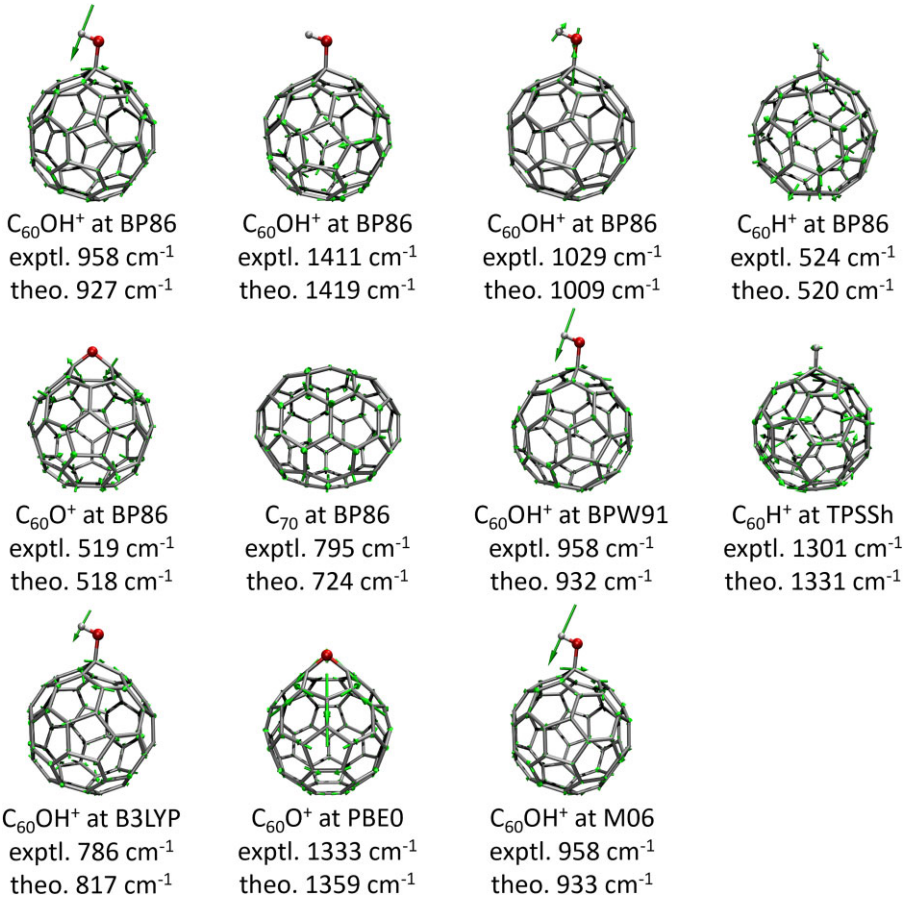

Figure A2. Selected vibrational vectors of modes at specific functional.

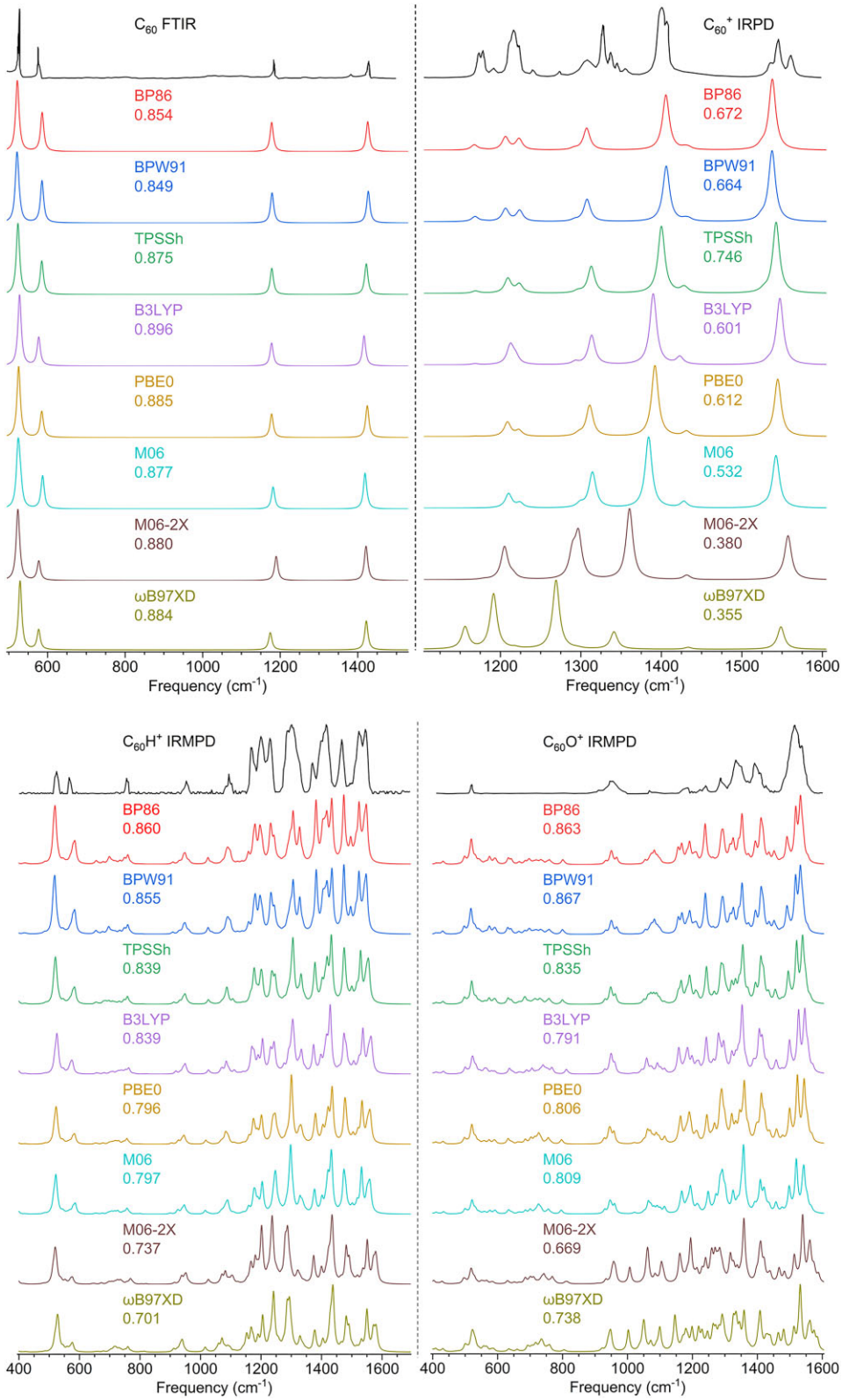

Figure A3. Performance of DFT functionals in predicting the infrared spectra. Comparison of scaled spectra with experimental measurements of C_{60}, C_{60}^+, $C_{60}H^+$, $C_{60}O^+$, $C_{60}OH^+$, C_{70}, $C_{70}H^+$, and $C_{60}V^+$ as digitized from Hare et al. (1991), Schettino et al. (2002), Gerlich et al. (2018), Palotás et al. (2019, 2021, 2022), and Hou et al. (2023). The spectra are convolved using Lorentzian line shapes of 10 cm^{-1} full width at half maximum, and calculated cosine similarity score for each functional is indicated.

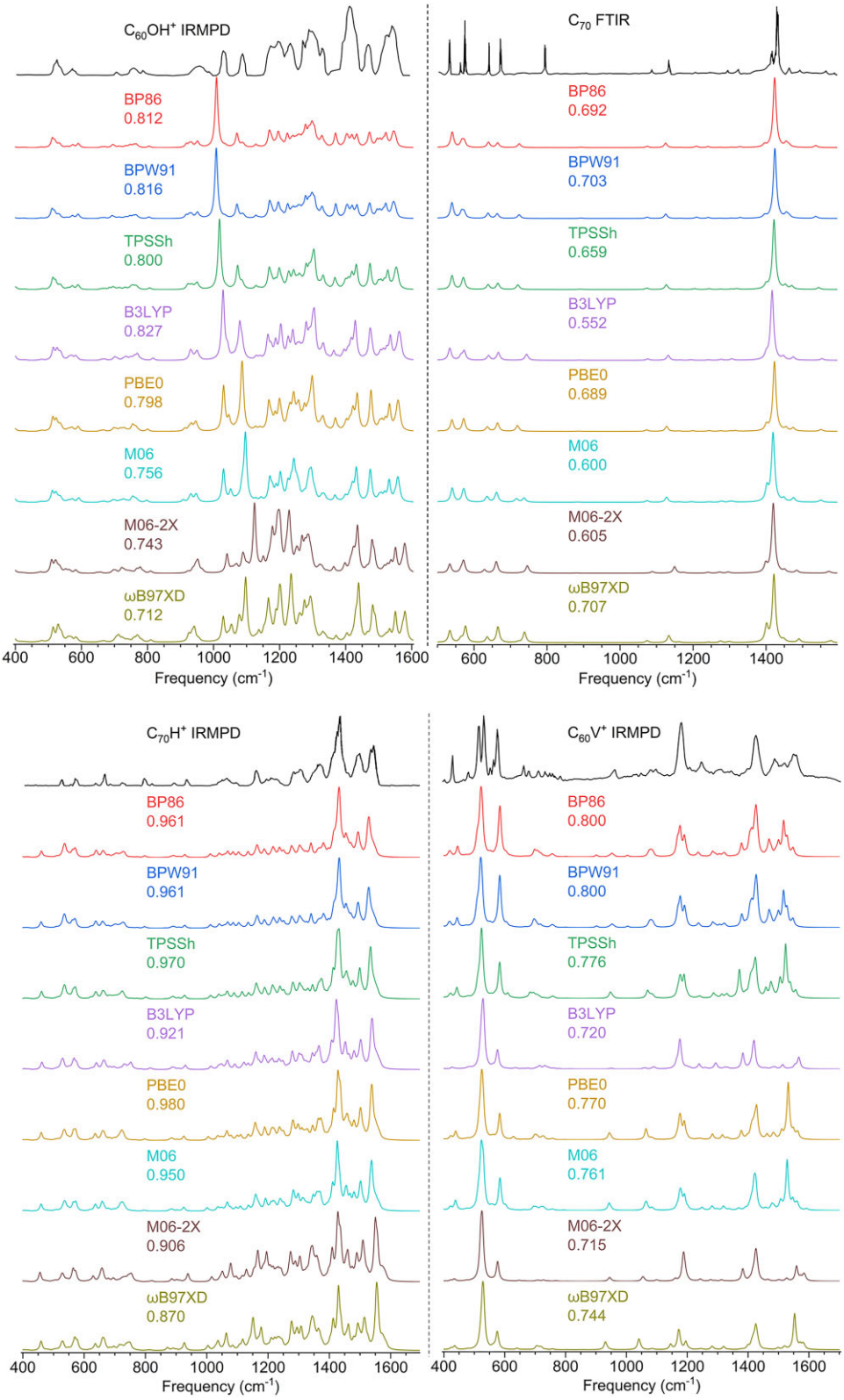

Figure A3. Continued.

Table A1. Fitting goodness of specific DFT functional. RMSE/median error values fitted using frequency-range-specific and global fitting strategies. The segmentation point of 50 cm^{-1} in the whole spectral range is used to determine the best-fitting results for a specific functional.

Seg. point	BP86	BPW91	TPSSh	B3LYP	PBE0	M06	M06-2X	ωB97XD
550	11.6/6.4	11.9/6.8	11.6/7.2	11.3/7.5	11.5/7.9	12.7/8.2	18.7/12.2	17.2/9.7
600	11.3/5.7	11.8/6.3	11.2/6.5	11.2/6.9	11.0/6.9	12.2/7.7	18.6/12.3	17.0/9.1
650	10.8/5.3	11.3/5.8	10.9/6.4	11.2/6.9	11.0/6.4	11.7/7.9	18.6/12.3	17.0/9.1
700	10.2/5.3	10.7/5.5	10.1/6.3	11.1/5.6	10.0/6.4	11.0/7.5	18.4/11.0	16.8/8.5
750	10.4/5.6	10.9/5.7	10.3/6.3	11.0/5.2	9.6/6.3	10.6/7.0	18.3/10.8	16.8/8.5
800	10.8/6.7	11.3/6.9	10.6/7.2	11.3/6.6	10.2/7.6	11.3/8.2	17.9/11.6	17.1/8.7
850	11.4/7.7	11.7/8.5	11.2/8.3	11.4/7.2	10.8/8.4	11.8/8.9	17.8/10.7	17.2/8.9
900	11.4/7.9	11.7/8.5	11.2/8.3	11.4/7.2	10.8/8.4	11.8/8.9	18.0/10.6	17.3/10.3
950	11.2/8.1	11.5/8.5	11.3/8.3	11.4/7.2	10.8/8.8	11.9/9.2	17.9/10.4	17.2/10.4
1000	11.3/8.1	11.7/8.2	11.1/8.3	11.4/7.2	10.7/8.4	11.6/9.2	17.8/9.6	17.1/9.2
1050	11.0/7.4	11.4/7.8	11.1/7.8	11.4/7.2	10.7/8.4	11.6/9.2	17.8/9.6	17.1/9.2
1100	11.4/7.6	11.8/7.6	11.1/7.7	11.3/6.9	10.6/8.2	11.6/9.4	17.5/9.9	16.9/9.5
1150	11.4/7.4	11.8/7.2	11.1/7.6	11.3/6.6	10.8/8.3	11.8/9.8	16.9/9.6	16.5/8.6
1200	11.8/7.2	12.0/6.2	11.3/7.6	11.3/6.7	10.8/8.3	12.4/9.0	17.4/9.4	16.7/9.5
1250	12.0/6.4	12.3/6.8	11.6/7.5	10.9/7.3	11.1/8.0	12.7/8.7	16.4/8.3	16.6/8.9
1300	11.8/6.1	12.3/6.6	11.9/7.5	11.3/7.0	11.4/8.0	13.0/8.5	16.5/10.3	16.4/9.5
1350	12.1/7.1	12.4/7.8	11.8/7.7	10.6/6.3	11.6/8.2	13.1/9.0	16.6/10.3	15.7/10.6
1400	12.2/6.7	12.5/7.5	12.1/8.2	11.3/7.0	11.5/7.6	13.1/9.6	15.6/10.2	16.1/9.5
1450	12.2/8.5	12.5/7.9	11.7/7.4	10.9/6.4	11.7/7.6	13.2/10.0	15.0/10.3	12.2/9.9
1500	12.1/7.5	12.4/7.5	12.1/8.3	11.2/6.5	11.6/7.0	12.8/8.7	15.4/10.0	15.1/9.6
1550	12.1/7.8	12.4/7.2	12.1/8.9	12.3/7.3	11.9/7.2	13.2/9.8	15.8/9.2	15.2/8.9
Global	12.3/7.0	12.5/7.4	12.1/8.0	11.4/7.3	12.0/7.9	13.3/9.4	18.8/12.5	17.3/9.6

This paper has been typeset from a TEX/LATEX file prepared by the author.